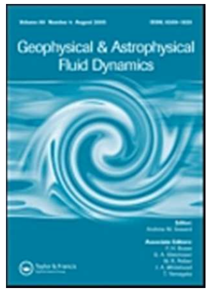

Convection Driven by Temperature and Composition Flux with the Same Diffusivity

Journal:	*Geophysical & Astrophysical Fluid Dynamics*
Manuscript ID	GGAF-2017-0007
Manuscript Type:	Original Article
Date Submitted by the Author:	16-Feb-2017
Complete List of Authors:	Whitehead, John; Woods Hole Oceanographic Institution, Physical Oceanography
Keywords:	double component convection, mixed boundary conditions, subcritical instability, pulsations

Convection Driven by Temperature and Composition Flux with the Same Diffusivity

J. A. Whitehead

Department of Physical Oceanography, Woods Hole Oceanographic Institution, Woods Hole, MA, USA,

Mail: MS#21, Physical Oceanography Department, Woods Hole Oceanographic Institution, Woods Hole, MA 02543, USA

email: jwhitehead@whoi.edu

This is in a form with figures and tables in appropriate places for reviewing

submitted to GAFD, 16 Feb 2017

Convection Driven by Temperature and Composition Flux with the Same Diffusivity

Abstract

Temperature, pressure, and composition determine density of fluids within the earth, the ocean, our atmosphere, stars and planets. In some cases, variation of composition component C competes equally with temperature T to determine buoyancy-driven flow. Properties of two-dimensional cellular convection are calculated with density difference between top and bottom boundaries determined by difference of temperature T (Dirichlet boundary conditions, quantified by Rayleigh number Ra that is positive destabilizing), fluxes of C (Neumann boundary conditions quantified by Raf that is positive destabilizing), and Prandtl number Pr. Numerical solutions in a 2-d rectangular chamber are analyzed for Prandtl numbers $Pr=1,\infty$. For Ra and $Raf>0$ and Raf above approximately 300, subcritical instability separates T-driven convection from C-dominated stagnation. The flow is steady but a sudden change in Ra or Raf produces decaying pulsations to the new flow. A boundary layer solution illustrates how the Neumann condition is less sensitive to flow speed than the Dirichlet condition. A new type of pulsating flow occurs for Ra and $Raf<0$. The pulsations are characterized by slow flow with weak compositional plumes in a thermally stratified flow interrupted by rapid flow with strong compositional plumes.

Keywords: double component convection, mixed boundary conditions, subcritical instability, pulsations

Word count: abstract 190, text 4451, references 268, figure captions

1. Introduction

All the large fluid bodies on earth, on some planets, on their moons, and in stars have more than one component contributing to density that drives or constrains the motion. Atmospheric air has temperature and moisture, ocean water has temperature and salinity, magmas and parts of the mantle have temperature and composition, the Earth's core has temperature and composition, planets and their moons have temperature and assorted components, and the sun has temperature and the helium/hydrogen ratio and some stars have the ratio of two or more elements with hydrogen.

The multi-component nature of the resulting flows is important and has led to development of specialized studies (e.g. double diffusion in the ocean, magmas, and stars, moist convection in the atmosphere, the dynamics of crystalline laden suspensions in magmas and liquid metals, and the behavior of hot turbidity flows in volcanic plumes). However, in many cases, the two components are not different because of internal processes, but because they are driven by different boundary conditions. For example the ocean surface temperature closely follows atmospheric temperature but the changes in salinity are driven by a flux of water across the ocean surface through evaporation, precipitation and land run-off. The temperature/salinity composition is a fundamental property of the ocean and it is linked to abrupt transitions of the thermohaline circulation regime (Broecker *et al.*, 1985; Boyle, 1990; Keigwin and Jones, 1994; Keigwin *et al.*, 1994; Bard *et al.*, 1996, Broecker, 1997; Stocker and Wright 1991, 2000; Burns *et al.,* 2003; Weart, 2003; and many others). The abrupt transitions are understood to arise as a direct consequence of different T and S time scales (Stommel 1961, Bryan 1986, Cessi 1994, Rahmstorf 1995, Manabe and Stouffer 1995, Rahmstorf and Ganopolski, 1999, Whitehead 1998; and Weaver *et al*. 1999, Hearn and Sidhu 1999, Bulgakov and Skiba 2003). In atmospheric circulation models, land and ocean surface temperatures are specified along with evaporative water flux. In cooling magmas or in metallurgy, the boundary T remains fixed at the solidification temperature but composition flux is determined by solidification processes. Early theoretical studies and laboratory studies of flows with different T and C boundary conditions arose in studies of the melting of ice in salt water, alloy formation and magma modeling (Huppert and Turner, 1981) but these generally focused on double diffusion effects (e.g. Turner 1973, Welander 1989,Tsitverblit and Kit 1993, Tsitverblit 1995).

In all of the "structured" models used to study these issues, (e.g. models with a specified internal structure such as box models or numerical models of ocean circulation with many internal processes parameterized), the internal mixing properties of T and C are set equal to each other so that double-diffusion or phase changes within the fluid are not relevant. An emphasis on the effect of the different boundary conditions alone in pure fluid dynamics problems was initiated by setting the diffusion of T and C equal (Tsitverblit 1997a,b, 1999, 2004, 2007) and Zhao *et al*. (2007). Tsitverblit (2007) describes these problems as "a fundamentally new class of hydro-dynamic instabilities underlying the formation of spatial and temporal flow patterns from a steady equilibrium state of spatially homogeneous fluid."

Some laboratory experiments illustrate the changes back and forth between T and C dominated flows driven by different boundary conditions. A chamber exposed to a temperature difference and a flux of salt water pumped steadily into a fresh water environment recovers the abrupt transitions and hysteresis of the original Stommel box model and a slightly more complex chamber produces a severely limited hysteresis range (Whitehead 2009). In other experiments, spontaneous oscillations back and forth between temperature and salinity driven flows occur (Whitehead *et al*. 2005).

This study presents some new results for the classical convection configuration initiated by Tsitverblit (2004) over much wider parameter ranges. A rectangular two-dimensional chamber contains fluid. A temperature difference is imposed between the top and bottom boundaries quantified by Rayleigh number Ra. A laterally uniform flux of composition C into or out of the chamber is imposed along the top and bottom boundaries quantified by the flux Rayleigh number *Raf*. Therefore temperature T is driven by Dirichlet boundary conditions and composition C is driven by Neumann boundary conditions. Zero flux boundary conditions are imposed on the lateral boundaries. Both infinite Prandtl number and *Pr*=1 cases are investigated with numerical calculations with free-slip boundary conditions on all boundaries over a wide range of positive and negative values of *Ra* and *Raf*.

2. Procedure

The Boussinseq equations of motion govern the flow.

$$\nabla' \cdot \tilde{u}' = 0 \tag{2.1a}$$

$$\rho_0 \frac{\partial \tilde{u}'}{\partial t'} + \rho_0 \left(\tilde{u}' \cdot \nabla'\right)\tilde{u}' == -\nabla' p' + \mu \nabla^2 u' + g\alpha\rho_0 T \hat{k} - g\beta\rho_0 S' \hat{k} \tag{2.1b}$$

$$\frac{\partial T'}{\partial t'} + \tilde{u}' \cdot \nabla' T' = \kappa \nabla'^2 T' \tag{2.1c}$$

$$\frac{\partial C'}{\partial t'} + \tilde{u}' \cdot \nabla' C' = \kappa \nabla'^2 C' \tag{2.1d}$$

In these equations, $\tilde{u}'$ is the velocity vector (prime denotes it is dimensional), T' is temperature, $\hat{k}$ is a unit vector in the direction of gravity directed downward in the z' coordinate direction and t' is time. The constants are: ρ_0 - average density, μ - viscosity, g - acceleration of gravity, α - linear coefficient of thermal expansion, β - linear coefficient of composition expansion, κ - thermal and composition diffusivity. The fluid is in a rectangular chamber of depth D and width W (figure 1). Average initial temperature of the fluid is T_0 and the temperature along the prescribed boundary is raised to a temperature distribution with the size $T_0 + \Delta T$ at t'=0. Simultaneously, average initial composition is zero and composition flux $Fc' = -\kappa\left[\partial C'/\partial z'\right]$ is imposed along the prescribed boundary.

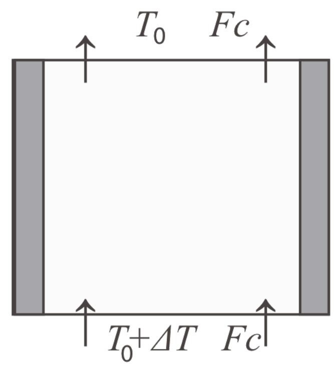

Figure 1. A rectangular container with constant temperature along the top, elevated temperature along the bottom and a uniform upward flux of composition. There is zero flux of heat and composition through the sides.

To non-dimensionalize, the velocity scale is set to κ/D, the scale of temperature in deviation from T_0 is ΔT, the composition scale is determined by the absolute magnitude of the derivative of composition imposed at the boundary $\Delta C = D\left|\partial C'/\partial z'\right|$, and time scale is D^2/κ. Henceforth, all dimensionless symbols are unprimed. Temperature and composition obey

$$\frac{\partial T}{\partial t} + \tilde{u}\cdot\nabla T = \nabla^2 T$$

$$\frac{\partial C}{\partial t} + \tilde{u}\cdot\nabla C = \nabla^2 C \quad . \tag{2.2a,b}$$

The equation governing vorticity $\zeta = \partial u/\partial z - \partial w/\partial x$ for two-dimensional right-handed Cartesian flow is

$$\left(\frac{1}{\mathrm{Pr}}\left(\frac{\partial}{\partial t} + \tilde{u}\cdot\nabla\right) - \nabla^2\right)\zeta = Ra\frac{\partial T}{\partial x} - Raf\,\frac{\partial C}{\partial x}\,, \tag{2.3}$$

and the equation for the stream function ψ where $u = \partial\psi/\partial z$ and $w = -\partial\psi/\partial x$ is

$$\nabla^2\psi = \zeta\,. \tag{2.4}$$

The three governing dimensionless numbers are Rayleigh number $Ra = g\alpha\Delta T D^3 / \kappa\nu$, composition flux Rayleigh number $Raf = -g\beta\left[\partial C'/\partial z'\right] D^4 / \kappa\nu$ and Prandtl number *Pr*.

The flow, temperature, and composition distributions are numerically calculated on a rectangular grid of points. Free slip boundary conditions are imposed on all four sides. For *Ra* and *Raf*>0, the chamber (figure 1) has bottom temperature ΔT above the top temperature, and composition flux F_C is upward and positive.

Initially, there is no motion and linear *T* and *C* profiles are specified in the interior to match the boundary conditions. The boundary conditions are *T*=0 across the top boundary and *T*=1 along the bottom. Composition flux is set to 1 along both the top and bottom. Equations (2.2a,b) are advanced numerically using a leapfrog-trapezoidal scheme for each time step δt. Then, (2.3) is solved either by stepping ahead in time as in (2.2) or, in the case of infinite *Pr,* using a standard Poisson equation solver with zero vorticity satisfied at all the boundaries. Then, (2.4) is solved using the Poisson solver with zero streamfunction at the boundaries.

Calculations at the four boundaries for flux using conventional second one-sided difference approximations in conjunction with the flux boundary conditions conserve *C* to the order of the numerical accuracy. The rectangular grid is two-dimensional with 128 points on a side giving an accuracy of 1 part in 10^6. Resolution was tested as in an earlier study (Whitehead *et al*. 2013) and all extrema of the fields are accurate to better than 1%. Since *C* has only flux boundary conditions, there is a slow random drift in the spatially averaged value of concentration $\bar{C}$ within the chamber over long times. If one-sided difference equations are used to calculate the flux into the system, the drift is a few parts in 10^{-6}. This drift is greatly decreased by using a better method. An external line of grid points is added outside each line of boundary grid points. This corresponds to a thin layer of solid around the chamber and in this layer the desired value of flux into the chamber is imposed by pure diffusion. Therefore, the variations of the value of flux into and out of the chamber occur at the numerical truncation order of 10^{-17}. Consequently, $\bar{C}$ randomly fluctuates about the mean to O (10^{-16}) (figure 2). Heat flow is also much more accurately preserved with this method since the sides are thermally insulated to the order of 10^{-17}.

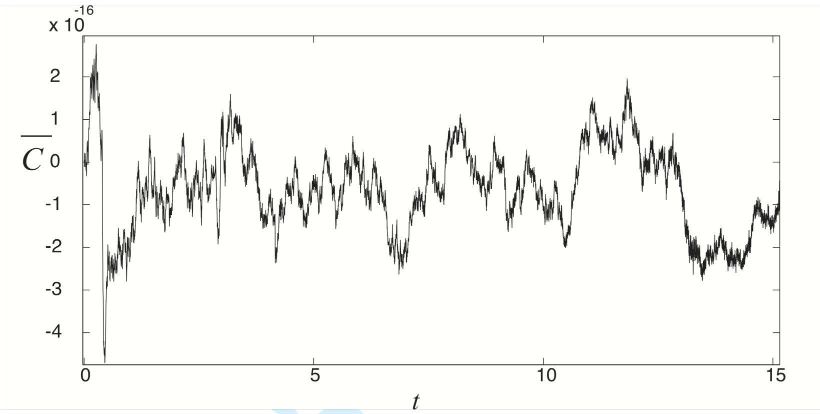

Figure 2. The value of mean composition remains at about one order of magnitude above the digital truncation level over a great span of time. This was obtained from the run shown in figure 3.

3. Results

Heated from below, stabilizing flux of composition

If we artificially set C =0 everywhere in the grid, there are well known flows. For example, the classical Rayleigh (1916) stability problem applies to this, and a boundary layer solution exists for a two-dimensional cell (Turcotte and Schubert 2002). With two components, the study by Tsitverblit 2004 shows that subcritical instability exists for *Raf* sufficiently large compared to *Ra*.

To determine stability of a flow, a calculation is started with a linear initial temperature and composition distribution. Temperature has the value 1 on the bottom that decreases linearly up to zero at the top, and composition has the same linear change but starts with the value 0.5 on the bottom and ends with -0.5 on the top. The initial state has exactly zero flow except that variations in each value of T and C at grid points exist at the truncation noise level of O (10^{-17}). This noise establishes a perturbation to the static fields. If *Ra* is large enough to make a disturbance linearly unstable, the perturbation grows. This is easily viewed by subtracting out the original linear distributions of T and C. With the 128x128 grid and a time step of 10^{-6}, the critical value of *Ra* found numerically with *Raf*=0 is

782. This is within the previously stated 1% of the correct value from linear theory for constant temperature free slip Rayleigh-Benard convection in a square box, which is $Rac=2^3\pi^4$=779.2727.

With a small value of *Raf* added, the growth of a small disturbance continues to be exponential in time. However, at larger *Raf*, the growth is oscillatory and exponential as shown in figure 3 for the maximum of the absolute value of streamfunction $|\psi|_{\max}$.

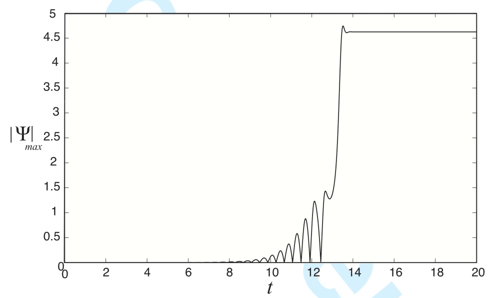

Figure 3. Evolution of the streamfunction for *Ra*=2200, *Raf*=1000, $Pr=\infty$.

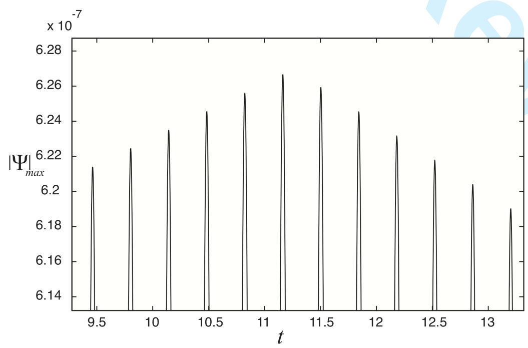

Figure 4. The peak amplitude of streamfunction versus time with two values of *Ra* spanning *Rac.* In the interval 9.3<*t*<11.3, *Ra*=2098 and the peaks increase with time. In the interval 11.3<*t*<13.3, *Ra*=2097 and the peaks decrease with time. *Raf*=1000, $Pr=\infty$.

Three types of runs determined critical parameter values and amplitudes. First, for very tiny amplitudes (e.g. before *t* =8 in figure 3) many successive runs are used to locate the largest possible value of *Ra* that has the fields decay in time. This is the critical Rayleigh number *Rac* for fixed *Raf* and *Pr*. The value of *Rac* is readily located by spanning successive values of *Rac*. An example for evolution of growing and decaying oscillations at two slightly different values of *Ra* for small (10^{-7}) amplitude is shown in figure 4. Values of *Rac* are rounded off to the nearest ten to be consistent with numerical accuracy and are shown in Table 1.

Raf	*Rac* (*Pr*=1)	*Rac* (*Pr*=∞)	*Ram* (*Pr*=1)	*Ram* (*Pr*=∞)
90	940 exp	940 exp	X	X
300	1270 exp	1270 exp	1260	1260
1000	2470 osc	2100 osc	1660	1660
10^4	9510 osc	10600 osc	6310	6620

Table 1. Values of the critical and minimum Rayleigh numbers and whether the growth of the very small flows is exponential or oscillatory.

The second type of run starts with steady flow at sufficiently large *Ra* and then sequentially decreases *Ra* by small amounts (e.g. figure 5) and waits for a sufficient time for amplitude to reach a steady value. The maximum absolute value of streamfunction for four values of *Raf* and two Prandtl numbers are shown in figure 6. Subcritical instability is very small but detected for *Ra*=300, and it clearly occurs for *Raf*=10^3 and 10^4. The minimum Rayleigh number for flow with a subcritical instability is called *Ram*, and values are shown in Table 1. For *Ra*=90 there is clearly no subcritical instability.

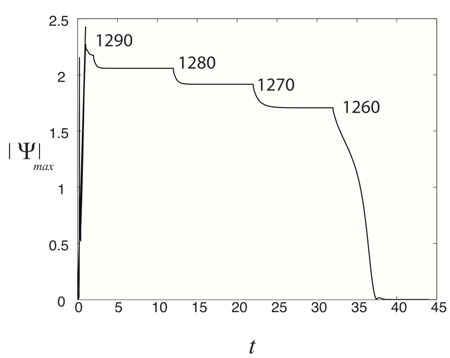

Figure 5. An example of the determination of successive values of the maximum value of streamfunction as *Ra* is slightly stepped down to the shown values. *Raf*=300, *Pr*=∞.

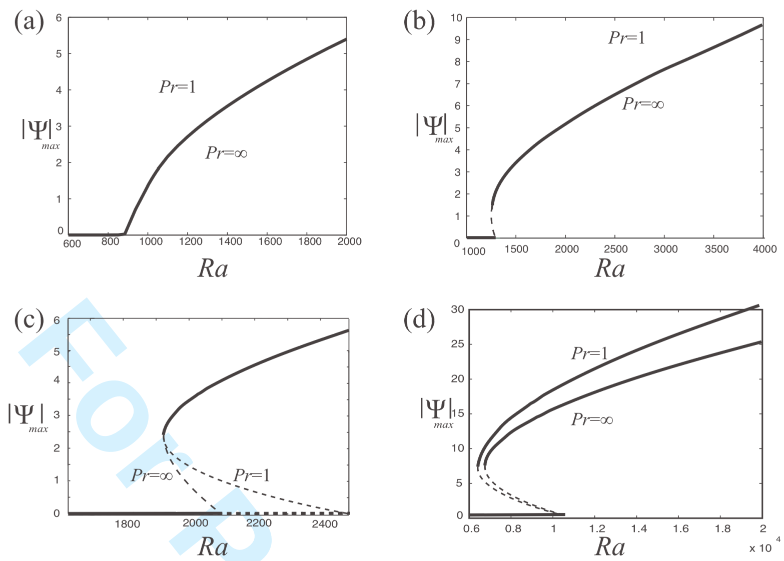

Figure 6. Speed versus the Direchlet variable *Ra* for the Neumann variables: (a) *Raf*=90, (b) *Raf*=300, (c) *Raf*=1000, and (d) *Raf*=10,000 and for *Pr*=1 and *Pr*=∞

The third type of run determines the unstable points (dashed lines in figure 6) using interrupted calculations. First, a calculation is started with *Ra* large enough to develop steady convection. Then, *Ra* is reduced to a value below *Ram* and $|\psi|_{\max}$ decays. When it reaches a desired value, *Ra* is changed so that it and $|\psi|_{\max}$ are close to a dashed line. After a short adjustment, if the magnitude is above the dashed line, $|\psi|_{\max}$ grows, and if it is below the dashed line, it decreases.

Large amplitude flow

For *Ra*=*Raf*=10^4 and for both cases with *Pr*=1 and *Pr*=∞, the temperature and composition distributions develop boundary layer structures. A typical example is shown in figure 7. The boundary layers bend at the corners to form *T* and *C* plumes along the sides that convey them vertically. The relative magnitudes in the plumes illustrate the effect of the two different boundary conditions. Temperature difference between the isothermal interior and each plume has magnitude 0.25 and the component difference is approximately ten times smaller. The flow pattern is almost the identical for both *Pr*=1 and ∞, except that the flow with large *Pr* is approximately 10% slower and accompanied by a slightly greater value *C* and smaller value of *T*. These results suggested that it is feasible to develop the boundary layer solution in section 4.

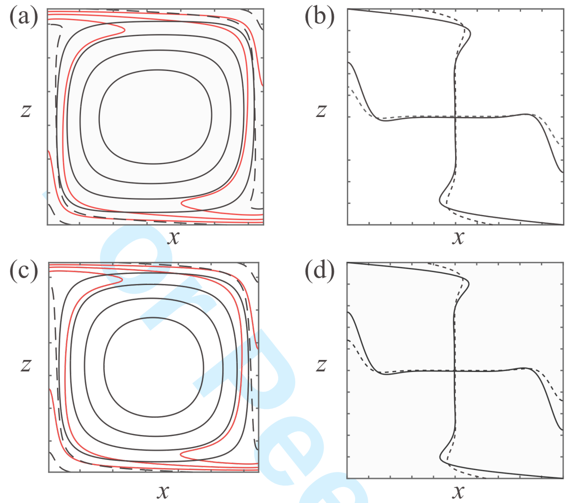

Figure 7. Temperature and composition for steady flow with $Ra=Raf=10^5$ and for $Pr=\infty$ (a,b) and for $Pr=1$ (c,d). (a,c) Vertical section showing isotherms (every T=0.2, red curves), composition (every C=0.02 , dashed lines) and steamfunction (solid contours every 0.2 units between $|\psi|_{\max}$ and zero). (b,d) Mid-cell vertical and horizontal profiles of T (solid) and of $5(C+0.5)$ (dashed).

Stabilizing temperature and destabilizing salt flux

With *Ra* and *Raf* set to negative values, salt flux drives the convection and heat flux stabilizes it. (For negative values, we use a negative symbol. Therefore, its value is positive and we avoid confusion with inequality signs). With Ra=0, the critical value of -*Raf* is 470.6234. The stability and flow characteristics for small -*Ra,* for example at $-Ra=10^2$, are not remarkable since a perturbation simply grows asymptotically to a steady flow, and subcritical instability is absent. New behavior exists for$-Raf>10^4$ (figure 8a). For example, with $-Raf=4\text{x}10^5$, pulsations separate a steady boundary layer driven flow at $-Ra<3\text{x}10^4$ and a layered stratified flow at $-Ra>2\text{x}10^5$. Pulsations are also present at $-Raf=10^5$, $8\text{x}10^5$ and 10^6. Amplitude of the flow with $-Raf=4\text{x}10^5$ (figure 8b) reflects the three distinct regions (figure 8b).

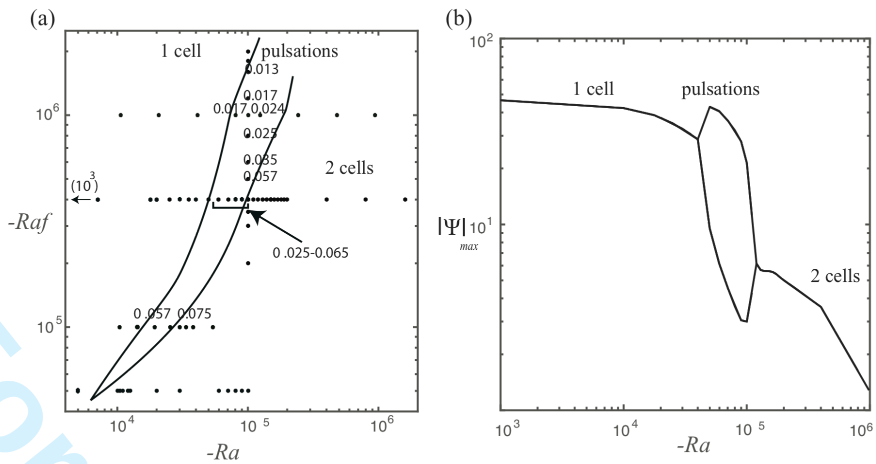

Figure 8. Summary of results for $Pr=\infty$. (a) Phase diagram of investigated values with the regions of different modes indicated. The periods of pulsations are given by the numbers. (b) The maximum absolute value of streamfunction for calculations with -Raf=4x10^5.

The three regions have different flow structures. The 1 cell flow has a boundary layer structure similar to the flow in figure 7 for the cases shown in this figure. Naturally, the density difference within the plumes is obviously dominated by C rather than T. For pulsations, the boundary layer flow speeds up and slows down at the smaller values of –Ra in the pulsation range. For example, along the line with -Ra=10^5 all the pulsations are like this. However, at larger –Ra (e.g. near the 2 cell transition), the flow oscillates back and forth between flow with 1 cell and flow with 2 cells. The flow patterns during one cycle alternating cells are shown in figure 9. Panels show: (a) At the beginning of a cycle, there are two cells at the two corners where the C plumes extend vertically from the horizontal surfaces. (b) These cells flow slowly enough to cause the composition in the boundary layer to gradually increase. (c) Soon thereafter, the plume density increases and this speeds everything up. (d) Faster flow produces one cell that is similar to the boundary layer flow shown previously in figure 7. (e) This rapid flow however causes a weakening of the concentration in the boundary layer and this weakening is greater than weakening of T. (f) This soon decreases density in the plumes and causes the single cell to divide into two slower cells. Therefore, the cycle repeats. One can summarize the shapes of the central contours of streamfunction as peanut-oval-circle-square- and peanut again.

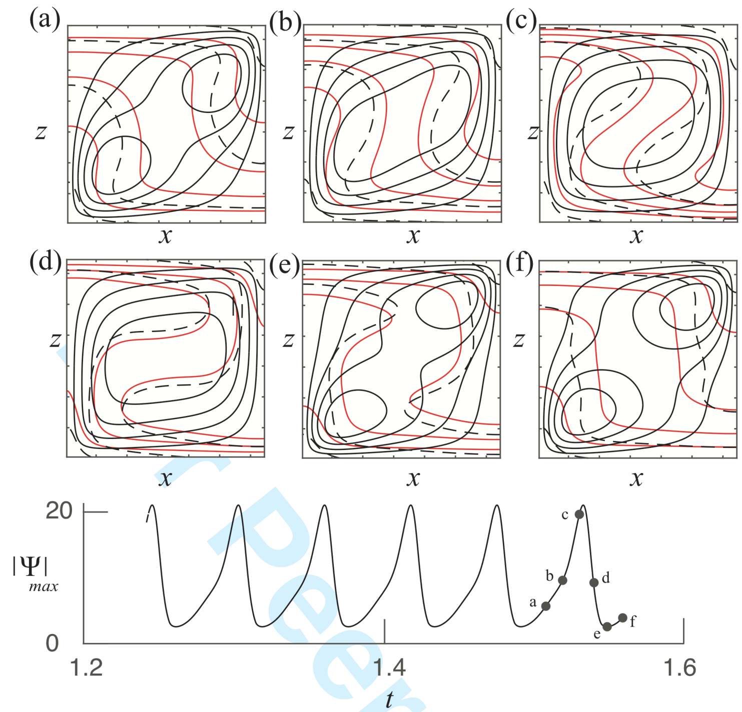

Figure 9. (Top) Contours of maximum absolute value of streamfunction (solid), T (red) and C (dashed) during the peanut-oval-circle-square-peanut pulsation sequence. Times are indicated in the bottom graph. $-Ra=10^5$, $-Raf=4\text{x}10^5$, $\Pr=\infty$.

The "two cells" region of figure 8 has one convection cell along the top and another along the bottom (figure 10). This begins to resemble a layered flow. At -*Ra* gets greater, the cells become more localized to the top and bottom and for -*Ra*=$1.5\text{x}10^6$ they have vanished.

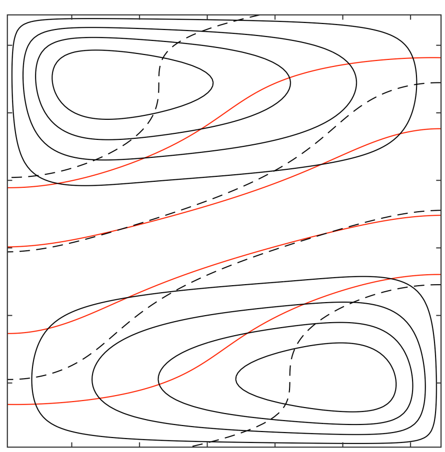

Figure 10. Contours of maximum absolute value of streamfunction (solid), T (red) and C (dashed) for layered steady flow at $-Ra= -Raf=4\text{x}10^5$.

4. Analysis

Pulsations

figure 11 shows extreme left minus extreme right mid-level grid points values for T(=T') and C' at the same points during a pulsation. First, C' follows T'. Second, C' is almost perfectly in phase with the streamfunction value.

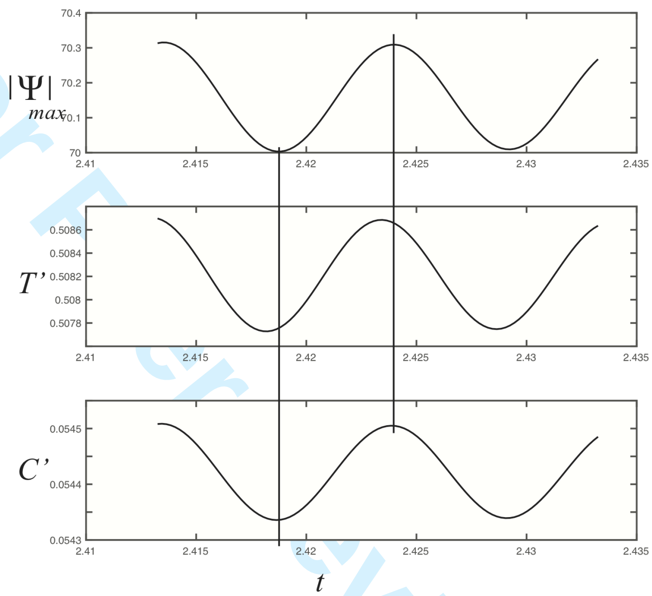

Figure 11. Maximum absolute value of streamfunction (top), T difference (middle) and C difference (bottom) during a pulsation cycle. $-Ra=10^5$, $-Raf=1.2\text{x}10^6$.

A simple way to picture why C' follows T' is to start with a simple model of a parcel of fluid that rotates around the edges of the convection cell and thus encounters alternating values of T and a flux of C at the outer edge. Consider the well-known thermal conduction solution of T from a sinusoidal time-varying temperature at y=0 next to a half-space. We take the variation to be in a y direction away from this boundary to avoid confusion with other sections. The solution is (Turcotte and Schubert eq. 4-89)

$$T = T_0 + \Delta T \exp\left(-y\sqrt{\frac{\omega}{2\kappa}}\right)\cos\left(\omega t - y\sqrt{\frac{\omega}{2\kappa}}\right) \quad . \qquad (4.1)$$

In our case, the gradient of C obeys the same differential equation. Therefore, the integral in y gives C as

$$C = C_0 + \frac{\partial C}{\partial y}\bigg]_{y=0} \sqrt{\frac{\kappa}{\omega}} \exp\left(-y\sqrt{\frac{\omega}{2\kappa}}\right)\cos\left(\omega t - y\sqrt{\frac{\omega}{2\kappa}} - \frac{\pi}{4}\right) \tag{4.2}$$

This shows how *T* follows *C*, as expected and it demonstrates that generally the two are not in phase for any pulsations at any flow rate. Naturally, this phase difference leads to the oscillation properties of this flow.

Boundary layer theory.

Let us construct a model of a convection cell driven by the boundary layers shown in figure 7. For simplicity, we modify the model of a convection cell from Section 6.21 of Turcotte and Schubert (2002) starting from our equations (2.2-2.4). The single cell has dimensionless length $L = \lambda'/2D'$ (the pair of cells has dimensional length λ'). A uniform velocity u_0 in the positive *x* direction exists across the top of this cell and a uniform velocity in the opposite direction exists across the bottom. Along the sides, the vertical velocity w_0 is uniform and upward on the left (x=0) and downward (negative) and uniform on the right (x=W). The temperature at the bottom (z=0) is T=1 and at the top (z=1) is T=0. The flux of salinity is 1 in the upward direction and this flux is uniform across both the bottom and top surfaces.

First the temperature field is calculated. The interior of the cell has closed circulation and the isothermal core has the average temperature T=0.5. A developing cold thermal boundary layer moves toward the right along the top and a developing warm thermal boundary layer moves toward the left along the bottom. Therefore, a plume of sinking cold fluid forms along the right side of the cell and a plume of rising warm fluid forms along the left side of the cell. The boundary layer temperature profile across the top is found by assuming uniform translation of fluid across the top with the fluid initially at T=0.5. Immediately under the top boundary, *T* obeys the well-known error function (Turcotte and Schubert 2002 equation 6-347)

$$T_{top} = 0.5 erfc\left(\frac{1-x}{2}\sqrt{\frac{u_0}{z}}\right) \quad . \tag{4.3}$$

The temperature distribution along the bottom is similar but it results from flow in the opposite direction and has higher temperature. It is

$$T_{bottom} = 1 - 0.5erf\left(\frac{x}{2}\sqrt{\frac{u_0}{z}}\right) \qquad (4.4)$$

where erf and erfc are respectively the error and complimentary error functions. The top boundary layer turns clockwise 90^0 at the upper right corner and forms a sinking cold plume. Likewise, the bottom boundary layer turns clockwise 90^0 at the lower left corner and forms a rising hot plume. We now estimate the total power P_T (rate of energy production) generated by buoyant thermal forces. It is given in dimensionless form by Ra times vertical velocity times density variation from the temperature deviation from its average value

$$P_T = Ra\int_0^1\int_0^L w(T - 0.5)\,dx\,dz\,. \qquad (4.5)$$

The principle contribution to P_T arises within the ascending and descending plumes. The plumes are also the principle contributors to vertical heat flux away from the boundaries, and since there is no internal heat generation in the fluid, the vertical heat flux is

$$Hf_T = \int_0^L wT\,dx \qquad (4.6)$$

and it is independent of z except near the bottom and top boundary layer regions. Since in this model it is assumed that vertical velocity is constant along the sides of the cell, any temperature profile can be used to determine the entire vertical integral of a plume and thereby evaluate (2.2a,b) throughout the interior. It is simplest to use the temperature profiles of the temperature fields that exist just before they turn the corner. As the fluid turns the bottom corner, for example, the vertical coordinate y in the boundary layer transforms to the lateral coordinate $z = w_0 x''/u_0$. Thus the body force in the ascending plume is (as in their equation 6-354)

$$f_{bT} = Ra\int_0^\infty erfc\left\{\frac{w_0 x''}{2u_0}\left(\frac{u_0}{L}\right)^{1/2}\right\}dx''$$

$$f_{bT} = Ra\frac{u_0}{w_0}\left(\frac{L}{u_0}\right)^{1/2}\int_0^\infty erfcz\,dz \tag{4.7}$$

$$f_{bT} = Ra\frac{u_0}{w_0}\left(\frac{L}{\pi u_0}\right)^{1/2}$$

The power driven by buoyancy is found by multiplying f_{bT} times vertical velocity w_0 over the depth (=1). A similar value is calculated from the top boundary layer that turns the corner and forms a descending plume. Therefore, total power from (4.5) is

$$P_T = 2Ra\sqrt{u_0 L/\pi}\,. \tag{4.8}$$

The contribution to the total power from concentration flux P_C is easy to calculate in a similar manner. The magnitude of the power is

$$P_C = Raf\int_0^1\int_0^L w(x,z)\left(C(x,z)-\bar{C}(z)\right)dx\,dz$$

The upward C flux per unit cell length equals 1, therefore a cell of length L has total upward C flux L. Concentration C forms structures similar to the thermal field, including boundary layers, plumes and an interior with a uniform value of C. For positive Raf the vertical work hinders convection and the power consumed is $P_C = -LRaf$. The total power is the sum of power from the two fluxes

$$P_{total} = 2Ra\sqrt{u_0 L/\pi} - LRaf\,. \tag{4.9}$$

This is balanced by frictional dissipation. In this simplified model of viscous flow, the velocity field has pure shear, so that

$$u = u_0(2z-1), w = w_0\left(1-2x/L\right) \tag{4.10}$$

The stress on the bottom is $2u_0$ per unit length and the dissipation at both bottom and top is equal to 2 times lateral velocity times stress times the length or $4u_0^2L$. The stress on the side is $2w_0/L$ and the stress for two sides times velocity is $4w_0^2/L$. Using the equation of continuity $u_0/L + w_0 = 0$ this becomes $4u_0^2/L^3$.

The power generation is equal to frictional dissipation and this gives the relation

$$2Ra\sqrt{u_0 L/\pi} - RafL = 4u_0^2\left(L + 1/L^3\right) . \tag{4.11}$$

For Raf=0, this reduces to equation 6-362 of Turcotte and Schubert (2002)

$$u_0 = \frac{L^{7/3}}{\left(1+L^4\right)^{2/3}}\left(\frac{Ra}{2\sqrt{\pi}}\right)^{2/3} \tag{4.12}$$

and for large values of Ra and Raf,

$$u_{0\,\min} = \frac{\pi L Raf^2}{4Ra^2} . \tag{4.13}$$

Solutions to (4.11) are visualized by plotting the right and left sides as a function of u_0 figure 12). The right side is a parabola extending upward from zero and the left side is a parabola on its side. For $Raf > 0$, the left side increases from a negative value. Solutions are intersection of such curves and they have a number of features:

1. For a fixed value of Ra, there is one value of Raf that corresponds to the minimum on the intersection curves. For Raf with a value greater than that, there is no solution.

2. Lower values of Raf have two intersections.

3. The intersection to the right is stable. A perturbation of smaller velocity there would follows a light curve lying above the dark curve. This produces more power release than dissipation and the consequent acceleration will increase velocity and cause a return to the intersection. A perturbation of a larger velocity also stabilizes by leading to less power release than dissipation. The deceleration produces slower flow and a return to the intersection.

4. The intersection to the left is unstable. The arguments are exactly opposite to case 3.

5. Convection driven by salinity (Raf<0) has light curves originating above zero. One solution exists and (4.11) indicates that wide cells are preferred.

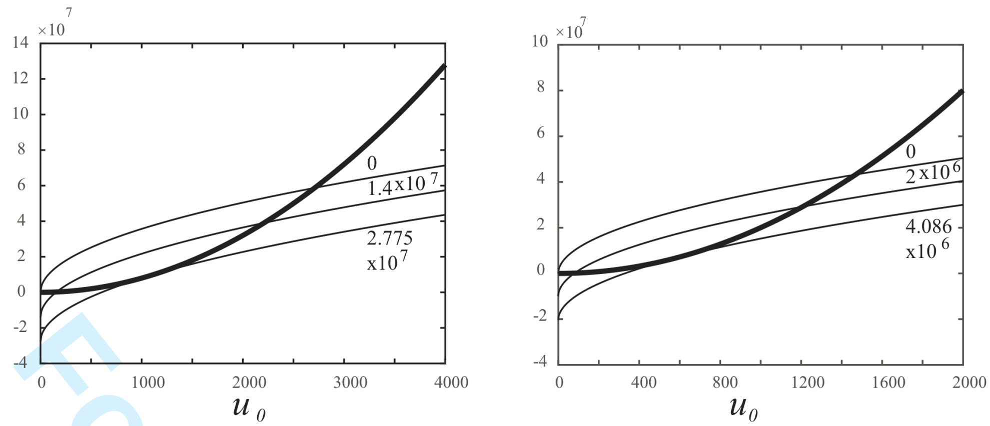

Figure 12. (a) The values of the right and left sides of (4.11) for $Ra=10^6$ and $L=1$. The solutions are intersections. The single thick parabola curving upward comes from the right hand side of (4.11). The three other curves come from the left hand side with three values of Raf . (b) The same for $L=5$.

The intersection of the two curves where there is only one value denotes the critical minimum value Ram for any Raf. If Ra is less than this value, no intersection is possible. The minimum value is found by rearranging (4.11) as

$$2Ra\sqrt{u_0L/\pi}-4u_0^2\left(L+1/L^3\right)=RafL \tag{4.14}$$

and noting that the term on the left has a maximum value with respect to u_0. Setting the derivative to zero, the velocity is

$$u_0=\frac{L^{7/3}Ra^{2/3}}{4\pi^{1/3}\left(1+L^4\right)^{2/3}} \tag{4.15}$$

and this gives a minimum value of Ra

$$Ram=\frac{4}{3}\sqrt{\frac{\pi}{L}}\left(1+L^4\right)^{1/4}Raf^{3/4}. \tag{4.16}$$

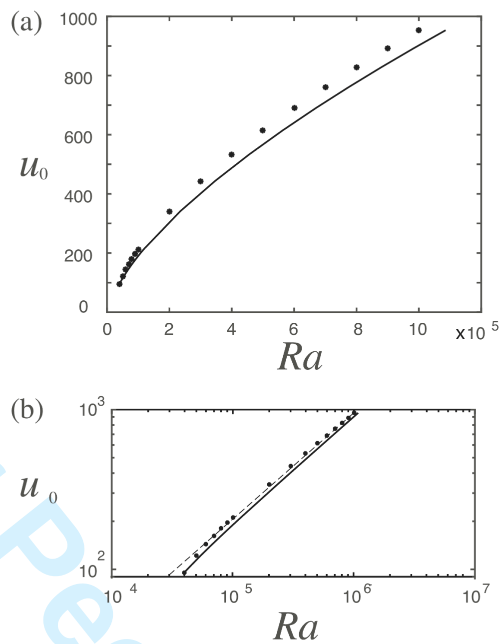

Figure 13. Velocity from numerical runs (dots) and from equation (4.13) (solid line) with *Raf*=10^5 and *L*=1. (a) Linear, (b) Log-log. The lightly dashed line is for *Raf*=0 (4.12) and it has been extended down to (4.16).

To compare these equations against the numerical results, first, comparison is made between (4.11) and results from numerical runs over the range *Ra*=30,000 to 10^6. Each numerical run was conducted with *Ra* and *Raf* specified and the peak velocity value is taken from the results. Analysis of many flows like the one shown in figure 7a,b found that this velocity is very close to the value $9|S|_{max}$. Therefore, these values are used in (4.11) to calculate a value of *Ra* to generate a curve for the boundary layer theory results. figure 13 shows the results. The actual and calculated values of *Ra* lie within 10% of each other. This comparison is surprisingly good considering that the model is very simple and many approximations are not strictly correct. The dashed line corresponding to convection with *Raf*=0 (4.12) is included in figure 13 and its slope matches. Therefore, the convection cell properties show little effect from compositional drag except near the transition region.

In contrast, a second test for the termination of the solution at small *Ra* using equation 4.16 does not compare well with numerical runs. The numerical run sequence in figure 13 had a termination of motion at *Ra*=32,000 while (4.16) gives *Ram*=14,707. It can be assumed that the poor agreement occurs because the boundary layer approximation breaks down in the vicinity of *Ram*.

5. Summary and Discussion

Finite amplitude instability and nonlinear oscillations occur for a convection cell driven by the two different boundary conditions. For positive *Ra* and *Raf*, the overall qualitative results are the same as found by Tsiverblit (2004). There is a range of subcritical instabilities if *Raf* is large enough. However, the quantitative agreement is not perfect. For example, Tsiverblit found the onset of subcritical instability for *Pr*=6.7 at *Raf* ~*Ra* to lie in the range *Ra*=120 to 240, but the present results produce an almost undetectable subcritical instability at *Ra*=300 for the two cases $\Pr = 1, \infty$. Also, we find that with *Raf*=10000, and *Pr*=1, *Rac* is 9600 whereas in Tsiverblit states that *Rac* goes to infinity for $\mu = Raf/Ra \rightarrow 1$. These differences between present and earlier quantitative values might be due to a number of factors: 1) Different values are given for *Pr*. 2) Cell wavelength differs. 3) A very accurate method of numerically incorporating the flux condition is used here. Finally, the subcritical instability resembles the subcritical instability in double diffusion (Veronis, 1964), but the exact overlap remains to be analyzed. The boundary layer solution gives a useful perspective on the role of the two different boundary conditions. With positive *Raf,* the speed abruptly ceases with decreasing *Ra*. The cut-off value does not have close quantitative agreement with *Ram* from numerical runs.

The parameter range *Ra* and *Raf* <0 produces pulsations for -*Ra*> 4×10^4. The pulsations differ from the oscillations at marginal stability in double diffusion (Veronis 1964, Turner 1973) and with multiple boundary conditions, (Welander 1989, Tsitverblit 2007), which occur for *Ra* >0 with stabilizing salinity present and in some thermohaline laboratory experiments (te Raa 2001, Whitehead *et al*. 2005). They are also unlike the binary fluid oscillations (Matura and Lucke 2006) that apparently are linked to double diffusion. Therefore, the pulsations seem to be new. One can look on the stabilizing temperature field as a spring that aids the pulsation. Their period is a small factor of the scaling timescale, so such pulsations might potentially arise in evaporative basins such as the Mediterranean Sea or the Red Sea. Like salt fingers, the new pulsations are novel dynamical structures with their own particular set of balances that may fruitfully be studied further.

The more accurate approach for a boundary layer flow by Vynnycky and Masuda (2013) requires more computation so it wasn't followed. The present solution gives good comparison with numerical results and its simplicity allows it to be used for teaching and to communication our basic understanding to less specialized people.

References

Bard E., Hamelin, B., M. Montaggioni, A. L., Cabiochparallel, G., Faure, G. and Rougerie, F. Deglacial sea-level record from Tahiti corals and the timing of global meltwater discharge. *Nature* 1996, **382**, 241 – 244.

Boyle, E. A., Quaternary deepwater paleoceanography. *Science,* 1990, **249**, 863–870.

Broecker W. S., Thermohaline circulation, the Achilles heel of our climate system: Will man-made CO_2 upset the current balance? *Science,* 1997, **278**, 1582–1588.

Broecker, W. S., Peteet, D. M. and Rind, D., Does the ocean–atmosphere system have more than one stable mode of operation? *Nature,* 1985, **315**, 21–26.

Bryan, F., High-Latitude composition effects and interhemispheric thermohaline circulations. *Nature,* 1986, **323**, 301–304.

Bulgakov S. N. and Y. N. Skiba, Are transitions abrupt in Stommel's thermohaline box model? *Atmosfera,* 2003, **16**, 205–229.

Burns, S. J., Fleitmann, D., Matter, A., Kramers, J. and Al-Subbary, A. A., Indian Ocean climate and an absolute chronology over Dansgaard/Oeschger events 9 and 13. *Science,* 2003 **201**, 1365–1367.

Cessi, P. A simple box model of stochastically forced thermohaline flow. *J. Phys. Oceanogr.,* 1994, **24**, 1911–1920.

Hearn, S. J. and Sidhu H. S., The Stommel model of shallow coastal basins. *Proc. Roy. Soc. (London)* A, 1999, **455**, 3997–4011.

Huppert, H. E., and Turner, J. S., Double-diffusive convection. *Journal of Fluid Mechanics,* 1981, **106,** 299-329.

Keigwin, L. D., Curry, W. B., Lehman, S. J. and Johnsen, S., The role of the deep-ocean in North-Atlantic climate-change between 70-Kyr and 130-Kyr ago. *Nature,* 1994, **371**, 323–326.

Keigwin, L. D. and Jones, G. A., Western North-Atlantic evidence for millennial-scale changes in ocean circulation and climate. *J. Geophys. Res.,* 1994, **99** (C6), 12,397–12,410.

Manabe, S. and Stouffer, R. J., Simulation of abrupt climate change induced by freshwater input to the North Atlantic Ocean. *Nature,* 1995, **378**, 165–167.

Rahmstorf, S., Bifurcations of the Atlantic thermohaline circulation in response to changes in the hydrological cycle. *Nature*, 1995, **378**, 145–149.

Rahmstorf, S. and Ganopolski, A., A. simple theoretical model may explain apparent climate instability. *J. Climate*, 1999 **12**, 1349–1352.

Stocker T. F., and Wright, D. G., Rapid transitions of the ocean's deep circulation induced by changes in surface water fluxes. *Nature*, 1991, **351**, 729–732.

Stommel H., Thermohaline convection with two stable regimes of flow. *Tellus*, 1961, **3**, 224–230.

Matura, P. and Lücke, M., Driving convection in a fluid layer by a temperature gradient or a heat current. *Physical Review E*, 2006 ***73*** (3), 037301.

te Raa, L., Convective oscillations in a laboratory model, GFD Fellows Report 2001, http://gfd.whoi.edu/proceedings/2001/PDF/rep_teraa.pdf

Tsitverblit, N. and Kit, E., The multiplicity of steady flows in confined double‐diffusive convection with lateral heating. *Physics of Fluids A: Fluid Dynamics*, 1993 ***5*** (4), 1062-1064.

Tsitverblit, N., Bifurcation phenomena in confined thermosolutal convection with lateral heating: Commencement of the double‐diffusive region. *Physics of Fluids*, 1995, ***7*** (4), 718-736.

Tsitverblit, N.A., The finger regime of double-diffusive convection with the equal diffusion coefficients and mixed boundary conditions. *Double-Diffusive Processes 1996 Summer Study Program in Geophysical Fluid Dynamics*, 1997a, Woods Hole Oceanographic Institution, 145.

Tsitverblit, N.A., On the nature of direct instabilities in double-component convection with different boundary conditions. *Physics of Fluids*, 1997b, **9** (8), pp.2458-2460.

Tsitverblit, N., Multiplicity of equilibrium states in laterally heated thermosolutal systems with equal diffusivity coefficients. *Physics of Fluids* 1999, **11** (9), 2516-2538.

Tsitverblit, N., Mechanism of finite-amplitude double-component convection due to different boundary conditions. *Physics Letters A*, 2004, ***329*** (6), pp.445-450.

Tsitverblit, N., Double-component convection due to different boundary conditions in an infinite slot diversely oriented to the gravity. *Annals of Physics*, 2007, ***322*** (8), 1727-1770.

Turner, J. S., *Buoyancy effects in fluids.* Cambridge University Press, New York, 1973, 367 pp.

Veronis, G., On finite amplitude instability in thermohaline convection, *J. Mar. Res.* 1964, **23**, 1

Weart, S., The discovery of Rapid Climate Change. *Phys. Today*, 2003, **56**, (8), 30–36.

Weaver, A. J., Bitz, C. M., Fanning A. F. and Holland, M. M., Thermohaline circulation: High-latitude phenomena and the difference between the Pacific and Atlantic. *Annu. Rev. Earth Planet Sci.,* 1999, **27**, 231.

Welander, P., A new type of double diffusive instability. Tellus 1989, **41**A, 66−72

Whitehead, J. A., Multiple T-S states for estuaries, shelves and marginal Seas. *Estuaries*, 1998, **21**, 278–290.

Whitehead, J. A., Abrupt Transitions and Hysteresis in Thermohaline Laboratory Models, *Journal of Physical Oceanography*, 2009, **39**, 1231-1243.

Whitehead, J. A., Cotel, A., Hart, S., Lithgow-Bertelloni, C. and Newsome, W., Numerical calculations of two-dimensional large Prandtl number convection in a box." *Journal of Fluid Mechanics* 2013, **729**, 584-602.

Whitehead, J. A., te Raa, L., Tozuka T., Keller, J. B. and Bradley K., Laboratory observations and Simple Models of Slow Oscillations in Cooled Salt-Stratified Bodies. *Tellus*, 2005, **57**A, (5) 778-809, doi:10.1111/j.1600-0870.2005.00150.x.

Zhao, F.Y., Liu, D. and Tang, G.F., Multiple steady flows in confined gaseous double diffusion with discrete thermosolutal sources. *Physics of Fluids*, 2007, ***19,*** (10), 107103.